UDC 621.793.1:621.9.02:620.18

V. I. Ivashchenko*, P. L. Scrynskyy, O. S. Lytvyn,
O. O. Butenko, O. K. Sinelnichenko (Kiev, Ukraine)
L. Gorb (Jackson, Vicksburg, USA)
F. Hill (Vicksburg, USA)
J. Leszczynski (Jackson, USA)
A. O. Kozak (Kyev, Ukraine)
**ivash@ipms.kiev.ua*

Comparative investigation of NbN and Nb–Si–N films: experiment and theory

NbN and Nb–Si–N films have been deposited by magnetron sputtering of the Nb and Si targets on silicon wafers at various powers supplied to the Nb target. The films have been investigated by an atomic force microscope, X-ray diffraction, X-ray photoelectron spectroscopy, nanoindentaion and microindentation. The NbN films were nanostructured, and the Nb–Si–N films represented an aggregation of δ-NbN_x nanocrystallites embedded into the amorphous Si_3N_4 matrix (nc-δ-NbN_x/a-Si_3N_4). The annealing of the films in vacuum showed that their intensive oxidation occurred at annealing temperature higher than 600 °C. To explain the experimental results on the Nb–Si–N films, first-principles molecular dynamics simulations of the NbN(001)/Si_3N_4 heterostructures have been carried out.

Keywords: *NbN and Nb–Si–N films, magnetron sputtering, film structure, bonding picture, nanoindentation, first-principles calculations, stress-strain curves.*

INTRODUCTION

Nanostructured films are widely used for surface hardening of cutting tools due to high hardness, good corrosion stability and low friction coefficient [1]. Among these films, NbN-based films are of increasing interest. The hardness of such binary NbN nitride films is much higher than the bulk material (H_V = 14 GPa) and higher than other binary nitride films (TiN, ZrN, VN). The hardness of the NbN films deposited by different arc deposition systems reaches 34–49 GPa [2–7]. The NbN films were also prepared by using magnetron sputtering (MS) [8–12], ion beam assisted deposition [13], pulsed laser deposition [14]. An increase in hardness was reached by the formation of the nanocomposite or nanolayered structures of the films based on niobium nitride [15–23]. Silicon nitrides are known for their high-temperature stability, low friction coefficient, and high oxidation resistance. Hence, one can expect that Nb–Si–N nanocomposite and multilayers will combine the properties of the constituent materials and will have improved properties as compared to NbN. In the following we will put an accent on the films prepared with magnetron sputtering. We reviewed the recent investigations into NbN and Nb–Si–N films deposited by magnetron sputtering. Some deposition parameters and hardness of these films are summarized in the table. One can see that the NbN system crystallizes with several different phases: δ-NbN (space group $Fm\bar{3}m$), ε-NbN (space group $P\bar{6}m2$) and δ′-NbN (space group $P6_3$/mmc) depend-

© V. I. IVASHCHENKO, P. L. SCRYNSKYY, O. S. LYTVYN, O. O. BUTENKO, O. K. SINELNICHENKO, L. GORB, F. HILL, J. LESZCZYNSKI, A. O. KOZAK, 2014

ing on deposition parameters. The formation of the hexagonal phases occurs at high nitrogen partial pressures and substrate biases [8–10, 12]. The hardness of the hexagonal δ′ and ε phases of NbN is higher compared to that of the cubic δ-NbN [8, 9].

Conditions of the deposition of NbN and Nb–Si–N films using magnetron sputtering (MS) technique and their mechanical properties.

Targets	Atmosphere	Varying parameter	Structure of NbN	Sub-strate	H, H_V, H_K, GPa	E, GPa	Ref.
			NBN films				
Nb	$Ar + N_2$	P_{N_2}, T_S	δ, δ′	Silicon wafer	$H = 25(δ)$ $H = 38(δ′)$	330(δ) 450(δ′)	[8]
Nb	$Ar + N_2$	P_{N_2}	δ, ε	Steel	$H = 30(δ)$ $H = 45(ε)$	400(δ) 650(ε)	[9]
Nb	$Ar + N_2$	U_B	δ, δ′	Silicon wafer	$H = 38$	–	[10]
NbN	$Ar + N_2$	T_S, $I_{NbN,}$ P_{N_2}	δ	Silicon wafer	–	–	[11]
Nb	$Ar + N_2$	P_{N_2}, U_B	δ, δ′	Steel	$H_K = 20.4$	–	[12]
			Nb–Si–N films				
Nb	$Ar + N_2 + SiH_4$	P_{SiH_4}	δ	Stainless steel	$H_V = 53$	–	[15]
Nb, Si	$Ar + N_2$	I_{Si}	δ	Silicon wafer	$H = 34$	330	[16–18]
Nb + Si	$Ar + N_2$	U_B	ε + δ	Silicon wafer	$H_V = 29$	–	[19]
Nb + Si	$Ar + N_2$	P_{N_2}	ε + δ	Silicon wafer	–	–	[20]

P_i is the partial pressure; T_S is the substrate temperature; I_i is the current supplied to an i target; U_B is the substrate bias; H, H_V and H_K are nanohardness, Vickers, and Knoop microhardness, respectively; E is the elastic modulus. δ-NbN (space group $Fm\bar{3}m$), ε-NbN (space group $P\bar{6}m2$) and δ′-NbN (space group $P6_3/mmc$) are cubic and hexagonal phases of NbN, respectively.

It was found that an addition of silicon up to 3.4 at % led to an increase in hardness up to 53 GPa [15]. This hardness enhancement was due to the specific nanocomposite structure of Nb–Si–N films that represented nano-sized NbN grains embedded in amorphous SiN_x matrix [15–20]. An increase in hardness from 25 to 34 GPa was explained in the framework of a two-step mechanism, i.e., by forming a solid solution of Si atom in NbN lattice and a nanocomposite material [16–18]. The hardness of Nb–Si–N nanocomposite films reaches the maximum values of 30–34 GPa for 5–13 at % of Si [17]. As in the case of NbN, for the Nb–Si–N system, high substrate biases and nitrogen partial pressures promote the growth of the ε-NbN grains [19, 20].

We see from this brief review that, despite the previous investigations of the NbN and Nb–Si–N films, the comparative study of these two kinds of films prepared at the same deposition parameters was not yet carried out. Also so far the effect of the discharge power supplied to the Nb target (P_{Nb}) on film properties was not analyzed. Besides, we note that, up to date, any theoretical investigations of the NbN/SiN_x nanostructures at the atomic level were not carried out.

In this work we aimed to fill these gaps in the investigations of NbN and Nb–Si–N films. These films were deposited on silicon wafers at various P_{Nb}. The films were then investigated by: an atomic force microscope (AFM), X-ray diffraction (XRD), X-ray photoelectron spectroscopy (XPS), nanoindentaion and microindentation. The deposited nanocomposite films were annealed to establish their thermal stability. The NbN(001)/Si_3N_4 heterostructures were calculated at various temperature using first-principles molecular dynamics simulations to interpret the experimental results on the Nb–Si–N films.

EXPERIMENTAL AND COMPUTATIONAL DETAILS

Experimental procedures

The NbN-based films were deposited on the mirror-polished Si (100) wafer by DC magnetron sputtering the Nb (99.9%, Ø72×4 mm) and Si (99.999%, Ø72×4 mm) targets in an argon-nitrogen atmosphere at the following deposition parameters: substrate temperature T_S = 350 °C; substrate bias U_B = –50 V; flow rate (F) F_{Ar} = 40 sccm; F_{N_2} = 13 sccm; working pressure p_C = 0.17 Pa. The current applied to the Nb target was 150, 200, 250 and 300 mA, which corresponded to a discharge power density P_{Nb} = 8.6, 11.4, 14.3 and 17.1 W/cm^2, respectively. The current on the Si target was 100 mA (P_{Si} = 5.3 W/cm^2). The base pressure of the vacuum chamber was better than 10^{-4} Pa. The distance between the targets and the substrate holder was 8 cm. The dihedral angle between the target planes was ~ 45°. The substrates were cleaned ultrasonically before they were put into the vacuum chamber. Also, before deposition, the substrates were etched in the vacuum chamber in hydrogen plasma during 5 min. The film deposited at P_{Nb} = 14.3 W/cm^2 was annealed in a vacuum (0.001 Pa) during 2 h at 600, 800 and 1000 °C.

The crystal structure of the films was determined by X-ray diffraction (XRD, diffractometer DRON-3M) using CuK_α radiation. The crystallite sizes in films were evaluated from the broadening of peaks in X-ray diffraction spectra using the Scherrer formula. The chemical bonding status of films was observed by X-ray photoelectron spectroscopy (XPS, EC 2401, USSR) using MgK_α radiation (E = 1253.6 eV). The Au4$f_{7/2}$ and Cu2$p_{3/2}$ peaks with binding energy at 84.0±0.05 eV and 932.66±0.05 eV, respectively, were used as references. Surface morphology was analyzed by an atomic force microscope (AFM) NanoScope IIIa Dimension 3000 (Digital Instruments, USA). The hardness and elastic modulus of films were determined from indentation by Nanoindenter-G200 instrument equipped with a Berkovich pyramidal tip under a load in the range of 9–13 mN. This range of loads was chosen in order to obtain prominent plastic deformation of a film while avoiding the influence of substrate material. The nanohardness (H) and elastic modulus (E) data were obtained from the load–displacement curves using the Oliver and Pharr method. The Knoop hardness (H_K) was estimated by a Microhardness Tester Micromet 2103 (BUEHLER Ltd.) at a load of 100 mN. The thickness of the films was determined with a Micron-Gamma optical profilometer. The thickness of the

films increased with P_{Nb}, from 0.8 to 1.1 μm (NbN films) and from 0.9 to 1.7 μm (Nb–Si–N films).

Theoretical methods

Atomic structures of the NbN(001)/Si_3N_4 heterostructures consisting of one Si_3N_4 interfacial monolayer (1 ML) between slabs of five NbN(001) layers were studied at 0 K and 1400 K in the framework of the first-principles quantum molecular dynamics (QMD) calculations with a subsequent static relaxation. We considered initial 96-atomic NbN supercell that was built by means of the translation of NaCl B1-type 8-atomic cubic cells in the *x*-, *y*-, and *z*-directions to form the (2×2×3) supercell. In this supercell, one Nb_8N_8(001) layer was replaced by the Si_6N_8(001) layer to model the NbN/$Si_{0.75}$N (NbN/Si_3N_4) nanostructures revealed in our experiments. We considered the (001) heterostructures since the Nb–Si–N films were found to be textured with the preferable (200) grain orientation.

The QMD calculations were performed with the quantum ESPRESSO code [24] using periodic boundary conditions and the generalized gradient approximation (GGA) of Perdew, Burke, and Ernzerhof (PBE) [25] for the exchange-correlation energy and potential. Vanderbilt ultra-soft pseudo-potentials were used to describe the electron-ion interaction [26]. The criterion of convergence for the total energy was 10^{-6} Ry/formula unit ($1.36 \cdot 10^{-5}$ eV/formula unit). In order to speed up the convergence, each eigenvalue was convoluted by a Gaussian with a width of $\sigma = 0.02$ Ry (0.272 eV).

The initial structure was optimized by simultaneously relaxing supercell basis vectors and atomic positions inside the supercell using the Broyden-Fletcher-Goldfarb-Shanno (BFGS) algorithm [27]. The QMD calculations of the initial relaxed heterostructure were carried out at 1400 K with fixed unit cell parameters and volume (NVT ensemble, constant number of particles-volume-temperature) for 1.7 ps. In the QMD calculations, the time step was 20 atomic units (about 10^{-15} s). The system temperature was kept constant by rescaling the velocity, and the variation of the total energy was controlled during each QMD time step. All structures reached their time-averaged equilibrium during the initial calculation time of about 1 ps, and afterwards, the total energy of the structures fluctuated only slightly around that equilibrium value. In the large-scale QMD simulation, the chosen reduced energy cut-off (30 Ry, 408 eV) and the k-points mesh (Γ point) were used in order to save computing time without compromising accuracy. The justification of such an approach was validated in [28, 29].

After QMD equilibration, the geometry of the heterostructure was optimized by simultaneously relaxing supercell basis vectors and positions of atoms inside the supercell using the BFGS algorithm [27]. The Monkhorst-Pack [30] (2×2×2) mesh was used. The relaxation of the atomic coordinates and supercell was considered to be complete when atomic forces were less than 1.0 mRy/Bohr (25.7 meV/Å), stresses were smaller than 0.05 GPa, and the total energy during the structural optimization iterative process was changing by less than 0.1 mRy (1.36 meV). For the generated 94-atoms heterostructures, we introduced the following abbreviation: "ZT" and "HT" refer to a 1 ML NbN(001)/Si_3N_4 heterostructures generated at 0 and 1400 K, respectively.

The tensile stress-strain relations were calculated by: 1) elongating the supercells along the *c*-axis [(001) direction] in an incremental step, 2) fixing the **c**-basis vector, and 3) simultaneously relaxing the **a**- and **b**-basis cell vectors and the positions of the atoms within the supercell. The shear stress of the heterostructures

under (100)[010] shear strains (parallel to the interface) was calculated as follows: first, an incremental shear distortion was imposed, then the dihedral angle between the **a** and **c** supercell vectors was fixed, and simultaneously the basis supercell vectors and the atomic coordinates were relaxed. For both tensile and shear strains the structural parameters at a previous step were used to calculate the Hellmann-Feynman stress for the next step.

The cubic B1-($Fm\bar{3}m$) NbN structure was studied to verify our computational method. The calculated lattice constant of a_{NbN} = 4.41 Å was found to be close to the experimental value of 4.394 Å, and comparable to other theoretical results of 4.378–4.42 Å [31].

RESULTS AND DISCUSSION

Experimental results

Figure 1 shows the AFM surface topography of the NbN and Nb–Si–N films deposited at various P_{Nb}. One can see that the film surface roughness increases with P_{Nb}. Also, the surface roughness in Nb–Si–N films is smaller than in NbN films, which can be due to the availability of the amorphous SiN_x tissue in Nb–Si–N films (see below). It follows that a decrease in the discharge power P_{Nb} and an introduction of silicon promote the reduction of surface roughness.

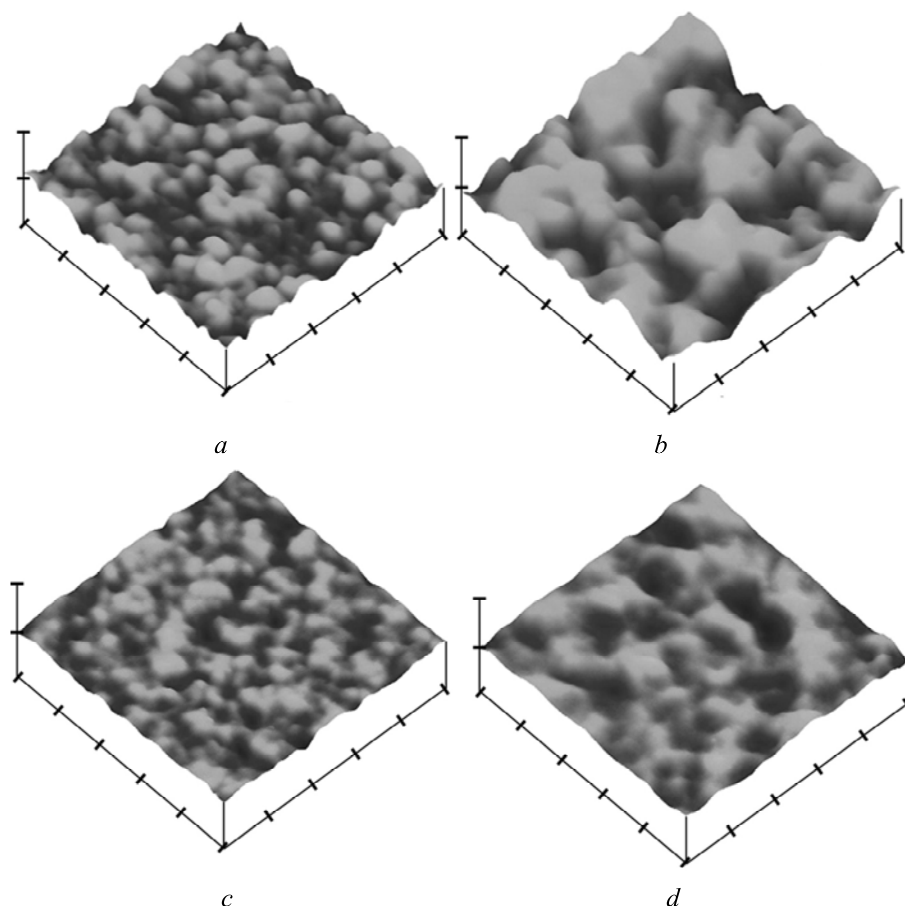

Fig. 1. AFM images of the NbN films deposited at P_{Nb} = 8.6 W/cm^2 (RMS = 4.2 nm) (*a*) and 14.3 W/cm^2 (RMS = 9.1 nm) (*b*); the Nb–Si–N films deposited at P_{Nb} = 8.6 W/cm^2 (RMS = 2.0 nm) (*c*), and 14.3 W/cm^2 (RMS = 2.8 nm) (*d*); *x* – 200 nm/div, *z* – 50 nm/div.

The XRD spectra of the deposited NbN and Nb–Si–N films are shown in Fig. 2. The A peak at 35.1–35.4° and the B peak at 41.1–41.4° can be assigned to the δ-NbN_x(111) and δ-NbN_x(200) reflections, respectively [32]. The grain size estimated from the Scherrer formula was in the ranges 4.1–8.7 nm and 18.1–19.8 nm for the NbN and Nb–Si–N films, respectively. It follows that an introduction of Si leads to an increase of the NbN grains. In Fig. 3 we show the dependences of grain size (D) of NbN and Nb–Si–N films on the parameter P_{Nb}. The value of D increases with P_{Nb} for Nb–Si–N and has an extreme dependence on P_{Nb} for NbN.

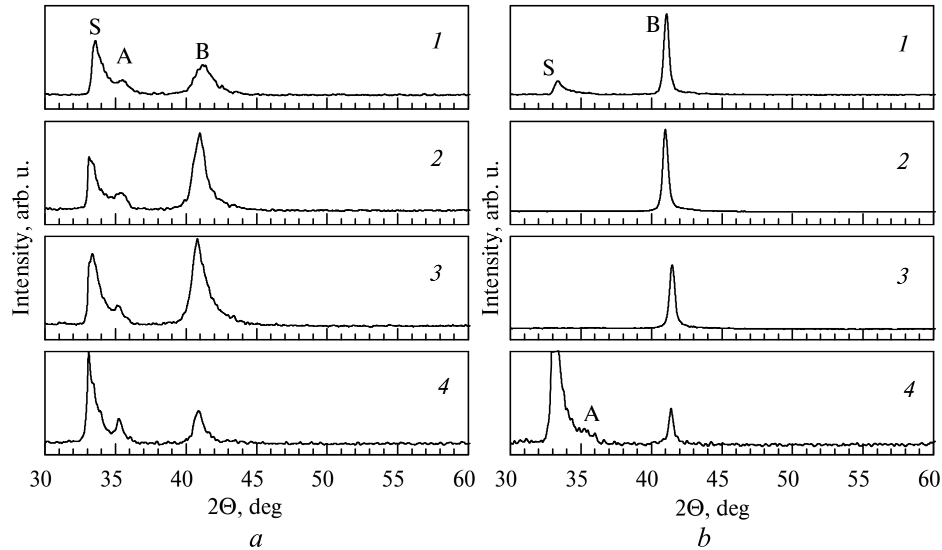

Fig. 2. XRD spectra of NbN (*a*) and Nb–Si–N (*b*) films. Denotation: S is silicon substrate reflex, A is δ-NbN(111) reflex, B is δ-NbN(200) reflex [24]; (*1*) 17.1 W/cm^2, (*2*) 14.3 W/cm^2, (*3*) 11.4 W/cm^2, (*4*) 8.6 W/cm^2.

The results of the XPS examination of as-deposited and annealed NbN and Nb–Si–N films are presented in Fig. 4. It is known that a native oxide grows on Nb compounds when exposed to air [19], and the peaks at 204.07 eV and 206.88 eV can be assigned to Nb3d in NbN (203.97 eV [21]) and $Nb_2N_{2\text{-}x}O_{3+x}$ (207.0 eV [33]). For NbN films, the peak at 397.4 eV in the N1s spectrum is determined by Nb–N bonds, whereas for Nb–Si–N films this peak is located around 397.2 eV and can be assigned to N1s in NbN (397.4 eV [19]). We suppose that the asymmetry of the N1s peak can be caused by the Si–N bonds in Si_3N_4 (397.8 eV [34]). XPS measurements of the Si2p spectrum provide further information on the Si bonding in the Nb–Si–N films (see Fig. 4). The peak at a binding energy of 101.7 eV is assigned to Si in Si_3N_4 (101.7 eV [34]), and a shoulder at 103.3 eV in the Si2p spectrum of the annealed films is supposed to be due to the Si–O bonds in SiO_2 (103.5 eV [34]). Finally, the O1s spectra of the NbN and Nb–Si–N films are centered around 530.5 eV and 530.9 eV, respectively, and can be attributed to the Nb–O bonds in Nb_2O_5 (530.4 eV) and Nb_2O_2 (530.7 eV [34]), respectively. In the case of Nb–Si–N films, the Si–O bonds in SiO_2 can form a wide tail around 532.9 eV [34] (see Fig. 4). Using the XPS data (see Fig. 4), we estimated the niobium, nitrogen, and silicon contents (C_{Nb}, C_N, and C_{Si}, respectively) in NbN and Nb–Si–N films. It was found that C_{Nb} = 44.5 at %, C_N = 55.5 at % for NbN films and and C_{Nb} = 45.1 at %, C_N = 43.2 at % and C_{Si} = 11.7 at % for Nb–Si–N films.

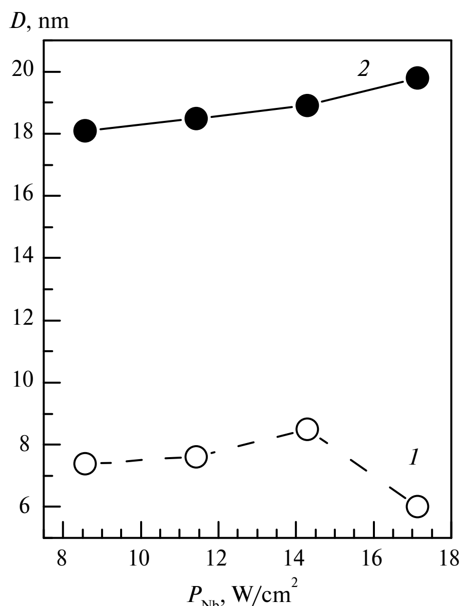

Fig. 3. Mean size of nanocrystallites *D*, estimated from the B peak using the Scherrer formula, as a function of the discharge power at the P_{Nb}; NbN (*1*), Nb–Si–N (*2*).

A comparison of the results presented in Figs. 1–4 enables us to establish the structure of the NbN and Nb–Si–N films. The NbN films are nanostructured, and the Nb–Si–N films have a nanocomposite structure, and represent an aggregation of δ-NbN_x nanocrystallites embedded into the amorphous Si_3N_4 tissue (nc-δ-NbN_x/a-Si_3N_4). In contrast to NbN films, Nb–Si–N films are textured with the preferable (200) grain orientation. The films contain oxygen as niobium oxides. For Nb–Si–N films we also suppose that oxygen forms SiO_2 that is segregated along grain boundaries. We note that despite the larger grain sizes, the surface roughness of the Nb–Si–N films is lower as compared to that of the NbN films. One can assume that the amorphous SiN_4 tissue in nanocomposite Nb–Si–N films smears the relief of the film surface. For this reason, the surface roughness of the nanocomposite films should be lower than that of NbN films.

The dependence of nanohardness (*H*) and elastic modulus (*E*) on indenter penetration (*L*) of the deposited films are presented in Fig. 5. It is seen that, beginning with 75 nm, the nanohardness practically does not depend on *L*. The elastic modulus decreases reaching the maximum values at $L = 50$ nm. These results point that the soft silicon substrate does not exert influence on the nanohardness of the films. The elastic modulus of the films turns out to be more sensitive to the substrates, especially at high *L*. In Fig. 6 we show the maximum values of *H* and *E*, determined from the *H*(*L*) and *E*(*L*) dependences, respectively, as well as the Knoop hardness (H_K) of the deposited films as functions of P_{Nb}. The nanohardness was found to be lower compared to the Knoop hardness approximately by 10–20 %. For NbN films, the values of *H* and H_K trend to increase with P_{Nb}. These values reach 28.3 and 36.1 GPa, respectively, for $D \sim 6$ nm (see Fig. 3). In the case of Nb–Si–N films, the maximum values of $H = 29.9$ GPa and $H_K = 44.2$ GPa are reached for $P_{Nb} = 11–14$ W/cm^2 ($D \sim 18.5–19$ nm). A comparison of the results presented in Figs. 3 and 6 shows that the elastic modulus of NbN and Nb–Si–N films increases with grain sizes. We note here that the structural and mechanical

properties of the deposited Nb–Si–N films are very close to those obtained in [15–18].

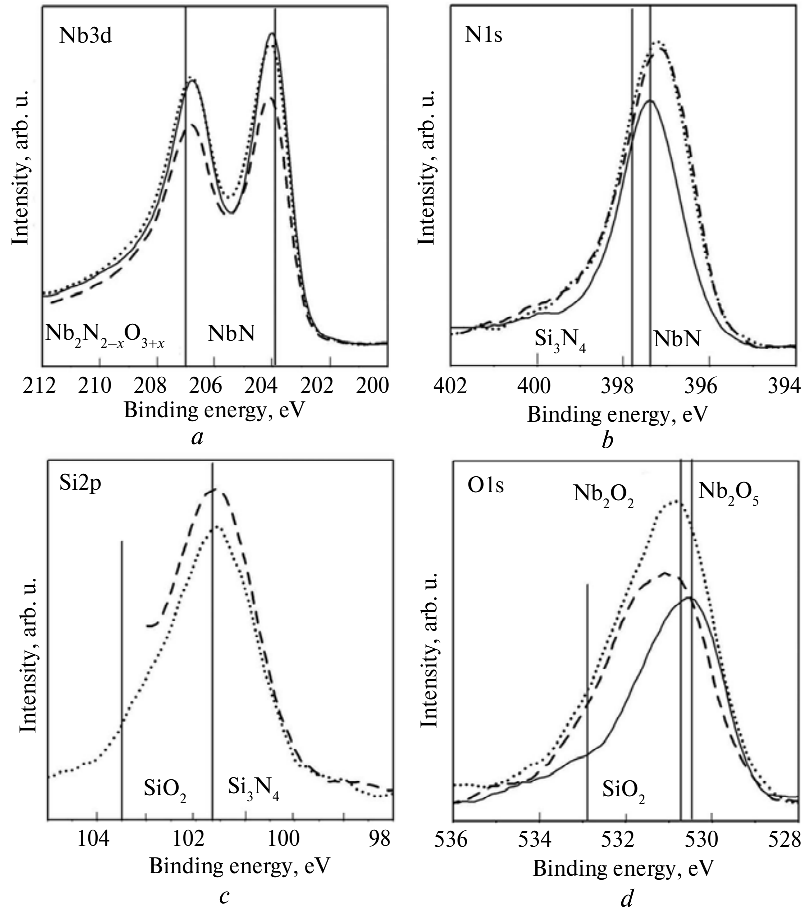

Fig. 4. XPS spectra of the core levels in NbN (solid line), Nb–Si–N (dashed line) and annealed at 1000 °C Nb–Si–N (dotted line) films deposited at P_w = 14.3 W/cm^2. The vertical lines denote the binding energies of the XPS peaks of: Nb3d in NbN, 203.97 eV [21] and $Nb_2N_{2-x}O_{3+x}$, 207.0 eV [33]; N1s in NbN, 397.4 eV [19], and Si_3N_4, 397.8 eV [34]; Si2p in Si_3N_4, 101.7 eV and SiO_2, 103.5 eV [34]; O1s in Nb_2O_5, 530.4 eV, Nb_2O_2, 530.7 eV, and SiO_2, 532.9 [34].

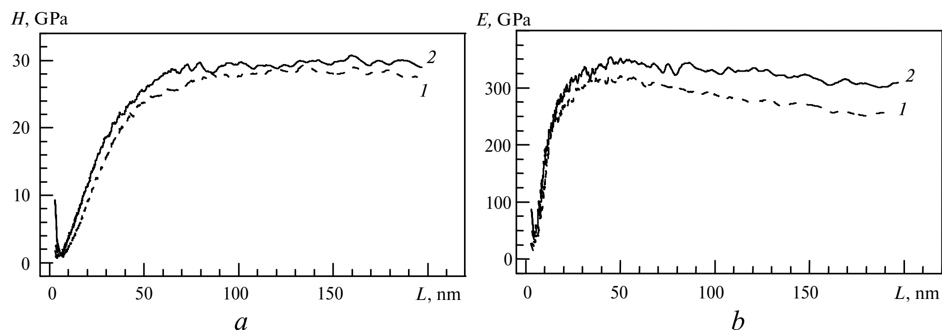

Fig. 5. Dependences of the nanohardness (*a*) and elastic modulus (*b*) on nanoindenter penetration for the NbN (*1*) and Nb–Si–N (*2*) films deposited at P_w = 17.1 W/cm^2.

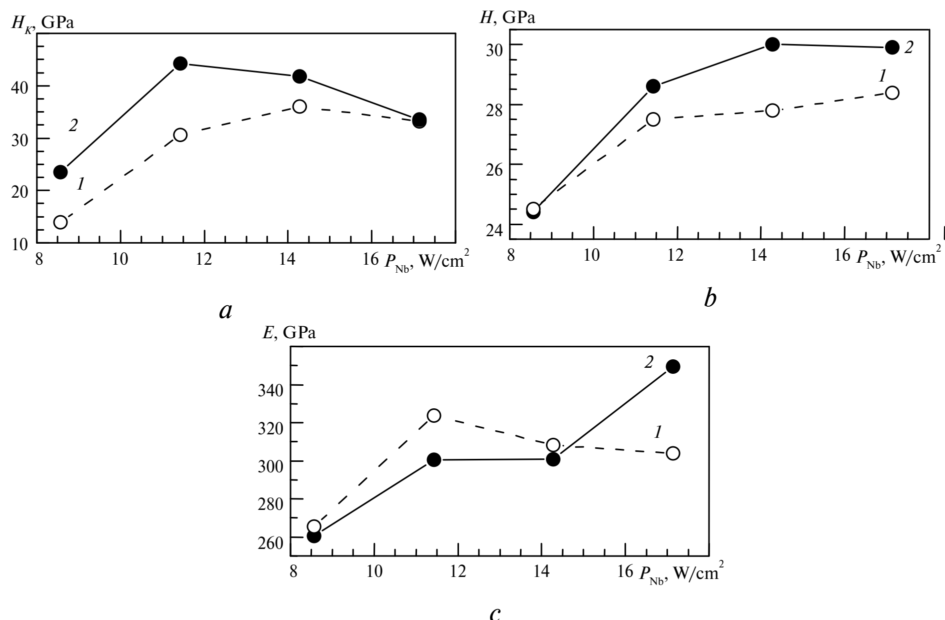

Fig. 6. Knoop hardness (*a*), nanohardness (*b*), and elastic modulus (*c*) as functions of the discharge power at the P_{Nb} for NbN (*1*) and Nb–Si–N (*2*) films.

Figure 7 shows the variation of the Knoop hardness of NbN and Nb–Si–N films with annealing temperature (T_a). The hardness slightly increases by annealing at T_a = 600 °C and decreases with further increasing T_a up to 1000 °C. The increase in hardness can be assigned to the densification of the coatings due to crystal rearrangements [21]. The significant lowering of H_K for T_a > 600 °C may be due to the oxidation, since the base vacuum inside the annealing chamber was maintained at 0.001 Pa. This vacuum is not low enough to prevent oxidation at high T_a. From Fig. 7 we see that the number of the Nb_2N_x and SiO_2 clusters increases after the annealing of the Nb–Si–N film at 1000 °C. The following reaction can govern the spontaneous oxidation of Si_3N_4 and NbN [21, 35]

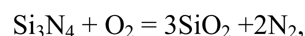

$$Si_3N_4 + O_2 = 3SiO_2 + 2N_2,$$

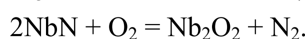

$$2NbN + O_2 = Nb_2O_2 + N_2.$$

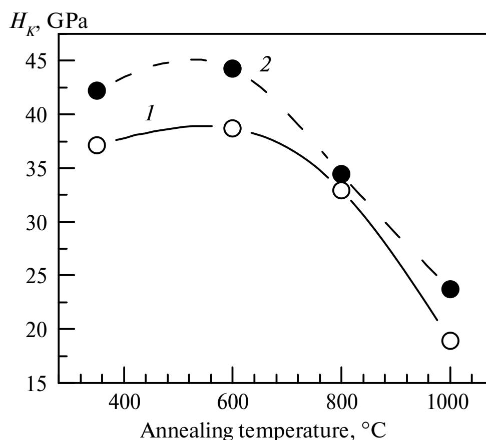

Fig. 7. Knoop hardness of the NbN (*1*) and Nb–Si–N (*2*) films deposited at 14.3 W/cm^2 as functions of annealing temperature. The point at 350 °C corresponds to the as-deposited film. The solid lines are the polynomial fit to the experimental points.

Theoretical results

In Fig. 8 we show the atomic configurations of the ZT and HT heterostructures. Figure 9 shows the arrangement of the atoms located on the (001) interfacial plane or close to it for the low- and high-temperature heterostructures. The geometry optimization of the initial B1-Si_3N_4 heterostructure at 0 K preserved the heteroepitaxial arrangement for the interface in a similar way as described for the TiN(001)/$Si_{0.75}N$ heterostructure [28]. The geometry of the (001) interface was preserved, but the nitrogen atoms above and below the interface were slightly shifted toward this interface. However, at 1400 K, the (001) interfacial structure significantly changed. Because the NbN(001)/Si_3N_4 heterostructure is strongly influenced by the temperature, we will consider it in detail. We note significant atomic re-arrangement caused by thermal motion of the interfacial atoms, which occurs predominantly within the interfacial layer. There are almost symmetrical, “down” and “up” shifts of the N atoms in the layer just above and below the interfacial layer, an almost random shift albeit of the Si atoms within the interfacial plane, breaking about half of the Si–N bonds. This leads to the formation of distorted over-coordinated Si_3N_4-like units that are represented by the SiN_4 and SiN_5 units (see Fig. 9). One can see from Fig. 9 that along with the new Si_3N_4-like units, some of the original six-fold coordinated B1-SiN_6 units are still present albeit distorted.

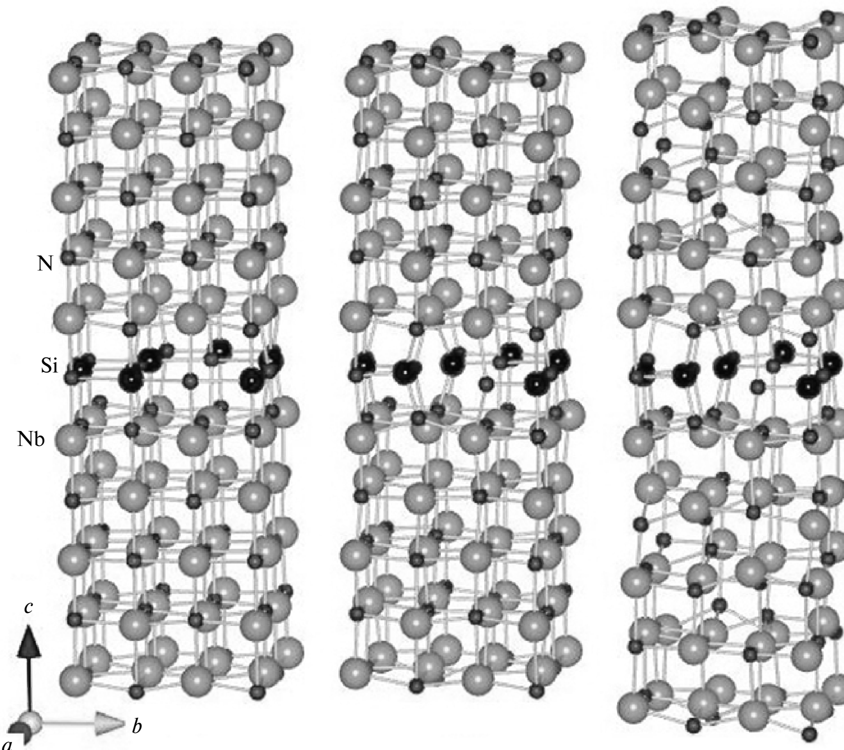

Fig. 8. Atomic configurations of the NbN(001)/$Si_{0.75}N$ heterostructures: (*a*) ZT at equilibrium, (*b*) HT at equilibrium, (*c*) HT under tensile strain $\varepsilon = 0.12$ (after failure). The bond length cutoffs were: 2.4 Å (Si–N) and 2.6 Å (Nb–N).

Because the Si–N bond length of 1.75–1.77 Å in β-Si_3N_4 is much shorter than the Ti–N bond length of 2.205 Å in pure NbN, there is a tensile misfit stress within the interfaces. This stress and the tendency of silicon to attain its four-fold

coordination to nitrogen as in Si_3N_4, which is the most stable configuration in the Si–N system, are the main factors that cause the reconstruction of the epitaxial layers. In Fig. 10, we present the pair correlation function (PCF) for the Si–N correlations. Figure 10 shows that the Si–N bond lengths of 1.79 Å correspond to the Si–N bonds in the distorted Si_3N_4-like units, whereas the peaks at 1.87 Å and 2.05 Å correspond to the Si–N bond lengths in the SiN_5 and SiN_6 units, respectively. A comparison of the structure and structural functions of the high-temperature interface in the NbN(001)/Si_3N_4 heterostructure with those of amorphous Si_3N_4 calculated in [28] show that the interface structure is very close to the structure of the over-coordinated amorphous Si_3N_4. So, the interface structure is not crystalline, and it is amorphous in agreement with the experiment.

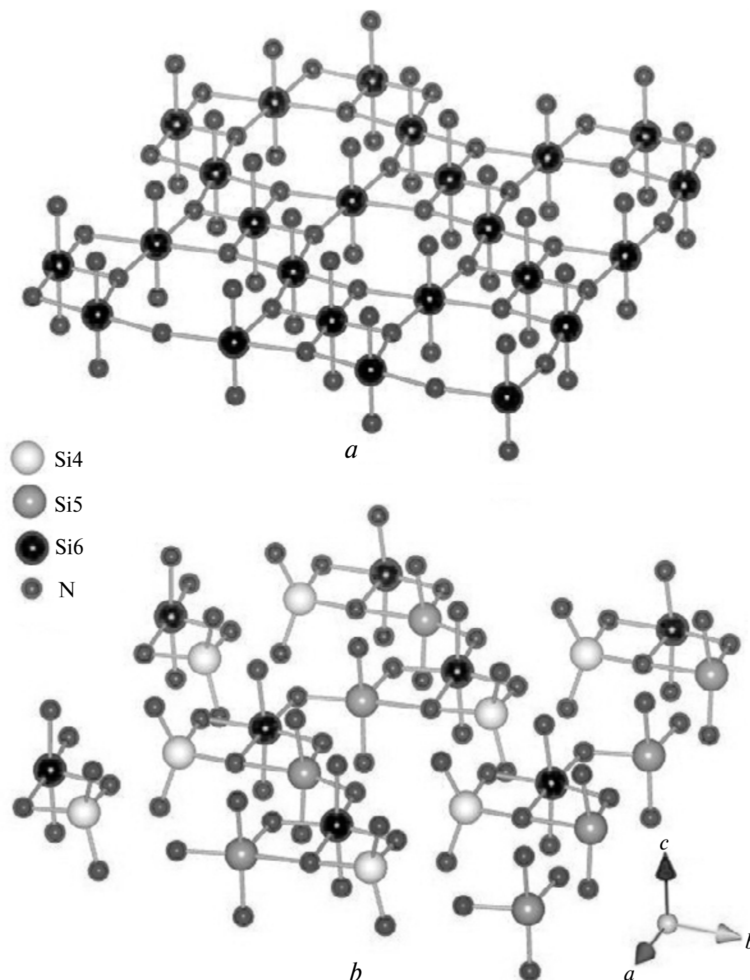

Fig. 9. Si–N network of the interfaces in: ZT (*a*) and HT (*b*) heterostructures. Si4, Si5, and Si6 are the four-fold, five-fold and six-fold coordinated silicon atoms, respectively. The bond length cutoffs were 2.4 Å.

The calculated stress-strain curves of the bulk NbN phase and the HT heterostructure under tensile strain (ε_t) in the (001) direction and shear (001)[010] strain (ε_s) are shown in Fig. 11. It is seen that the formation of the Si_3N_4 interface in NbN leads to a reduction of the ideal tensile strength. The atomic configuration of the HT heterostructure after failure under tensile strain is presented in Fig. 8, *c*.

The delamination occurs inside the NbN slab: the bonds are broken between the NbN layers adjacent to the interface. The shortening of the Si–N bonds causes an elongation of the Nb–N ones between these layers, for which reason they will be broken under tensile strain in the first place.

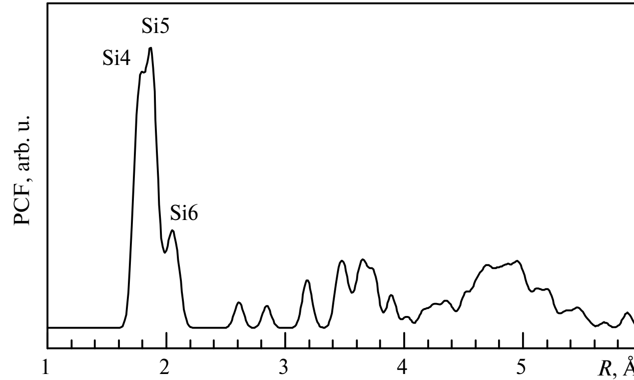

Fig. 10. Si–N pair correlation functions for the HT heterostructure.

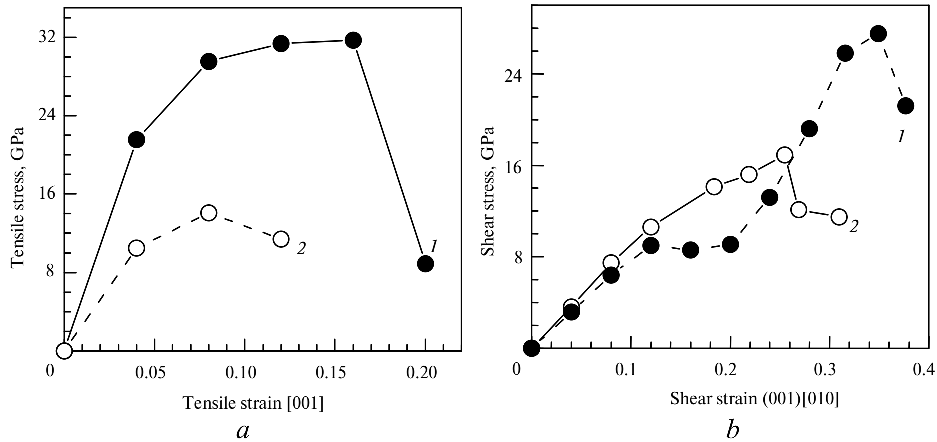

Fig. 11. Calculated stress-strain curves for the bulk NbN (*1*) and the HT NbN(001)/Si_3N_4 heterostructure (*2*); tensile (*a*); shear (*b*).

For pure NbN, in the range of $0.12 \leq \varepsilon_s \leq 0.2$, the shear stress is practically independent of the strain (see Fig. 11). We suppose that such a plastic region in the stress-strain curves is due to the dynamical instability of the stoichiometric B1-NbN caused by the availability of the soft transverse acoustics $X_{5'}$ modes [36, 37]. Nevertheless, despite this plastic region, the ideal shear strength of NbN is higher compared to that of the HT NbN(001)/Si_3N_4 heterostructure (see Fig. 11).

Thus, it follows from these findings that the formation of the interfacial Si_3N_4-like layer in δ-NbN(001) destabilizes niobium nitride. Interface formation does not result in strengthening of the nanocomposites from a chemical bonding perspective. For the NbN(001)/Si_3N_4 heterostructures, in the absence of lattice defects (dislocations, point defects, etc.), our theoretical results predict the reduction in both hardness and elastic modulus with the formation of the NbN(001)/Si_3N_4-like interface in δ-NbN. Therefore, the observed strength enhancement in the nc-δ-NbN/a-Si_3N_4 nanocomposite coatings (see Fig. 6) should

be ascribed mostly to the interfaces that play the role of barriers inhibiting dislocation motion.

CONCLUSIONS

We have deposited the NbN and Nb–Si–N films on silicon wafers by magnetron sputtering at various discharge powers applied to the Nb target, P_{Nb}. The comparative investigation of the deposited films has been carried out. AFM investigations show that a decrease in the discharge power P_{Nb} and an introduction of silicon promote the reduction of the surface roughness of the films. The XRD and XPS examination enabled one to establish the possible structure of the deposited films: the NbN films were nanostructured, and the Nb–Si–N films had a nanocomposite structure, and represented an aggregation of δ-NbN_x nanocrystallites embedded into the amorphous SiN_x tissue (nc-δ-NbN_x/a-Si_3N_4). In contrast to NbN films, Nb–Si–N films are textured with the preferable (200) grain orientation. The Nb–Si–N films exhibit the higher hardness (H ~ 30 GPa, H_K ~ 44 GPa) than NbN films (H ~ 28 GPa, H_K ~ 36 GPa) mainly due to the formation of the nanocomposite nc-δ-NbN_x/a-Si_3N_4 structure. The elastic moduli of NbN and Nb–Si–N films increase with grain sizes. The Knoop hardness of the films decreases with increasing annealing temperature above 600 °C due to the oxidation of NbN and Si_3N_4.

The results of first principles molecular dynamics simulations of the NbN(001)/Si_3N_4 heterostructures show that in the absence of lattice defects the interface formation does not result in strengthening of the nanocomposites. Therefore, the observed strength enhancement in the nc-δ-NbN/a-Si_3N_4 nanocomposite coatings should be ascribed mostly to the interfaces that play the role of barriers inhibiting dislocation motion.

This work was partially supported by STCU Contract No. 5539. The authors are grateful to Dr. Timofejeva, I. I. and Dr. Dub, S. N. for XRD investigations and nanoindentation of the films. The authors are grateful to the directorate of the Summery Institute at Jackson State University for financial support and the possibility to perform large-scale calculations.

NbN і Nb–Si–N плівки осаджували на кремнієві пластини методом магнетронного розпилення мішеней Nb і Si при різних потужностях розряду на мішені із Nb. Плівки були досліджені за допомогою атомно-силового мікроскопа, дифракції рентгенівських променів, рентгенівської фотоелектронної спектроскопії, нано- і мікроіндентування. NbN плівки були наноструктуровані, тоді як Nb–Si–N плівки являли агрегацію δ-NbN_x нанокристалітів, вкраплених в аморфну Si_3N_4 матрицю (nc-δ-NbN_x/ a-Si_3N_4). Відпал плівок у вакуумі показав, що їх інтенсивне окислення відбувається при температурі вищій, ніж 600 °C. Для пояснення експериментальних результатів по Nb–Si–N плівках проведено моделювання NbN (001)/Si_3N_4 гетероструктури із перших принципів в рамках молекулярної динаміки.

***Ключові слова**: NbN і Nb–Si–N-плівка, магнетронне розпилення, структура плівки, картина зв'язків, наноіндентування, розрахунки з перших принципів, напружено-деформаційні криві.*

NbN и Nb–Si–N пленки осаждали на кремниевые пластины методом магнетронного распыления мишеней Nb и Si при различных мощностях разряда на мишени с Nb. Пленки были исследованы с помощью атомно-силового микроскопа, дифракции рентгеновских лучей, рентгеновской фотоэлектронной спектроскопии, нано- и микроиндентирования. NbN пленки были наноструктурированные, тогда как Nb–Si–N пленки представляли агрегацию δ-NbNx нанокристаллитов, вкрапленных в аморфную Si_3N_4 матрицу (nc-δ-NbNx/a-Si3N4). Отжиг пленок в вакууме показал, что их интенсивное окисление происходит при температуре выше, чем 600 °C. Для объяснения экспериментальных

результатов по Nb–Si–N пленках проведено моделирование NbN (001)/Si_3N_4 гетероструктуры из первых принципов в рамках молекулярной динамики.

Ключевые слова: *NbN- и Nb–Si–N-пленка, магнетронное распыление, структура пленки, картина связей, наноиндентирования, расчеты из первых принципов, напряженно-деформационные кривые.*

1. *Veprek S.* Recent attempts to design new super- and ultrahard solids leads to nano-sized and nano-structured materials and coatings // J. Nanosci. Nanotechnol. – 2011. – **11**. – P. 14–35.
2. *Andrievski R. A., Anisimova I. A., Anisimov V. P.* Structure and microhardness of TiN compositional and alloyed films // Thin Solid Films. – 1991. – **205**. – P. 171–175.
3. *Martin P. J., Bendavid A.* The filtered arc process and materials deposition // Surf. Coat. Technol. – 2001. – **142–144**. – P. 7–10.
4. *Bendavid A., Martin P. J., Kinder T. J., Preston E. W.* The deposition of NbN and NbC thin films by filtered vacuum cathodic arc deposition // Surf. Coat. Technol. – 2003. – **163–164**. – P. 347–352.
5. *Zhitomirsky V. N., Grimberg I., Rapoport L. et al.* Structure and mechanical properties of vacuum arc-deposited NbN coatings // Thin Solid Films. – 1998. – **326**. – P. 134–142.
6. *Boxman R. L., Zhitomirsky V. N., Grimberg I. et al*. Structure and hardness of vacuum arc deposited multi-component nitride coatings of Ti, Zr and Nb // Surf. Coat. Technol. – 2000. – **125**. – P. 257–262.
7. *Zhitomirsky V. N.* Structure and properties of cathodic vacuum arc deposited NbN and NbN-based multi-component and multi-layer coatings // Surf. Coat. Technol. – 2007. – **201**. – P. 6122–6130.
8. *Benkahoul M., Martinez E., Karimi A. et al.* Structural and mechanical properties of sputtered cubic and hexagonal NbN_x thin films // Ibid. – 2004. – **180–181**. – P. 178–183.
9. *Fontalvo G. A., Terziyska V., Mitterer C.* High-temperature tribological behaviour of sputtered NbN_x thin films // Ibid. – 2007. – **202**. – P. 1017–1022.
10. *Wen M., Hu C. Q., Wang C. et al.* Effects of substrate bias on the preferred orientation, phase transition and mechanical properties for NbN films grown by direct current reactive magnetron sputtering // J. Appl. Phys. – 2008. – **104**, art. 023527.
11. *Alfonso J. E., Buitrago J., Torres J. et al.* Influence of fabrication parameters on crystallization, microstructure, and surface composition of NbN thin films deposited by r.f. magnetron sputtering // J. Mater. Sci. – 2010. – **45**. – P. 5528–5533.
12. *Singh K., Bidaye A. C., Suri A. K.* Magnetron sputtered NbN films with Nb interlayer on mild steel // Int. J. Corrosion. – 2011. – **2011**, art. ID 748168.
13. *Hayashi N., Murzin I. H., Sakamoto I., Ohkubo M*. Single-crystal niobium nitride thin films prepared with radical beam assisted deposition // Thin Solid Films. – 1995. – **259**. – P. 146–149.
14. *Cappuccio G., Gambardella U., Morone A. et al.* Pulsed laser ablation of NbN/MgO/NbN multilayers // Appl. Surf. Sci. – 1997. – **109**. – P. 399–402.
15. *Dong Y., Liu Y., Dai J., Li G.* Superhard Nb–Si–N composite films synthesized by reactive magnetron sputtering // Appl. Surf. Sci. – 2006. – **252**. – P. 5215–5219.
16. *Benkahoul M., Sandu C. S., Tabet N. et al.* Effect of Si incorporation on the properties of niobium nitride films deposited by DC reactive magnetron sputtering // Surf. Coat. Technol. – 2004. – **188–189**. – P. 435–439.
17. *Sandu C. S., Benkahoul M., Sanjinés R., Lévy F.* Model for the evolution of Nb–Si–N thin films as a function of Si content relating the nanostructure to electrical and mechanical properties // Ibid. – 2006. – **201**. – P. 2897–2903.
18. *Sandu C. S., Sanjinés R., Benkahoul M. et al.* Formation of composite ternary nitride thin films by magnetron sputtering co-deposition // Ibid. – 2006. – **201**. – P. 4083–4089.
19. *Wang J., Song Z., Xu K.* Influence of sputtering bias on the microstructure and properties of Nb–Si–N films // Ibid. – 2007. – **201**. – P. 4931–4934.
20. *Song Z. X., Wang Y., Wang C. J. F. et al.* The effect of N_2 partial pressure on the properties of Nb–Si–N films by RF reactive magnetron sputtering // Ibid. – 2007. – **201**. – P. 5412–5415.
21. *Jeong J. J., Lee C. M.* Effects of post-deposition annealing on the mechanical and chemical properties of the Si_3N_4/NbN multilayer coatings // Appl. Surf. Sci. – 2003. – **214**. – P. 11–19.
22. *Jeong J. J., Hwang S. K., Lee C.* Hardness and adhesion properties of HfN/Si_3N_4 and NbN/Si_3N_4 multilayer coatings // Mater. Chem. Phys. – 2003. – **77**. – P. 27–33.

23. *Wen M., Meng Q. N., Hu C. Q. et al.* Structure and mechanical properties of δ-NbN/SiN_x and δ′-NbN/SiN_x nano-multilayer films deposited by reactive magnetron sputtering // Surf. Coat. Technol. – 2009. – **203**. – P. 1702–1708.
24. *Giannozzi P., Baroni S., Bonini N. et al.* QUANTUM ESPRESSO: a modular and open-source software project for quantum simulations of materials // J. Phys.: Condens. Matter – 2009. – **21**, art. 395502.
25. *Perdew J. P., Burke K., Ernzerhof M.* Generalized gradient approximation made simple // Phys. Rev. Lett. – 1996. – **77**. – P. 3865–3868.
26. *Vanderbilt D.* Soft self-consistent pseudopotentials in a generalized eigenvalue formalism // Phys. Rev. B. – 1990. – **41**. – P. 7892–7895.
27. *Billeter S. R., Curioni A., Andreoni W.* Efficient linear scaling geometry optimization and transition-state search for direct wavefunction optimization schemes in density functional theory using a plane-wave basis // Comput. Mater. Sci. – 2003. – **27**. – P. 437–445.
28. *Ivashchenko V. I., Veprek S., Turchi P. E. A., Shevchenko V. I.* Comparative first-principles study of TiN/SiN_x/TiN interfaces // Phys. Rev. B. – 2012. – **85**, art. 195403.
29. *Wang S., Gudipati R., Rao A. S. et al.* First-principles calculations for the elastic properties of nanostructured superhard TiN/Si_xN_y superlattices // Appl. Phys. Lett. – 2007. – **91**, art. 081916.
30. *Monkhorst H. J., Pack J. D.* Special points for Brillouin-zone integrations // Phys. Rev. B. – 1976. – **13**. – P. 5188–5192.
31. *Isaev E. I., Simak S. I., Abrikosov I. A. et al.* Phonon related properties of transition metals, their carbides, and nitrides: A first-principles study // J. Appl. Phys. – 2007. – **101**, art. 123519.
32. *X-ray* powder diffraction file [089-5007].
33. *Darlinski A., Halbritter J.* On the identification of interface oxides and interface serration by ARXPS // Fresenius Z. Anal. Chem. – 1987. – **329**. – P. 266–271.
34. *Beamson G., Briggs D*. High Resolution XPS of Organic Polymers: The Scienta ESCA 300 Database. – John Wiley & Sons, Chichester, 1992. – 306 p.
35. *Jouve G., Severac C., Cantacuzene S.* XPS study of NbN and (NbTi)N superconducting coatings // Thin Solid Films. – 1996. – **287**. – P. 146–153.
36. *Christensen A. N., Dietrich O. W., Kress W. et al.* Phonon anomalies in transition metal nitrides: δ-NbN // Sol. St. Commun. – 1979. – **31**. – P. 795–799.
37. *Ivashchenko V. I., Turchi P. E. A., Olifan E. I.* Phase stability and mechanical properties of niobium nitrides // Phys. Rev. B. – 2010. – **82**, art. 054109.

Frantsevich Institute for Materials Science Problems,
National Academy of Sciences of Ukraine
Lashkarev Institute of Physics of Semiconductors,
National Academy of Sciences of Ukraine
Interdisciplinary Center for Nanotoxicity, Jackson State University, Jackson, USA
Badger Technical Services, LLC, Vicksburg, USA
U.S. Army ERDC, Vicksburg, USA

Received 01.04.14